

Chapter 1

Present Status in the Development of III–V Multi-Junction Solar Cells

Simon P. Philipps, Wolfgang Guter, Elke Welser, Jan Schöne, Marc Steiner, Frank Dimroth, and Andreas W. Bett

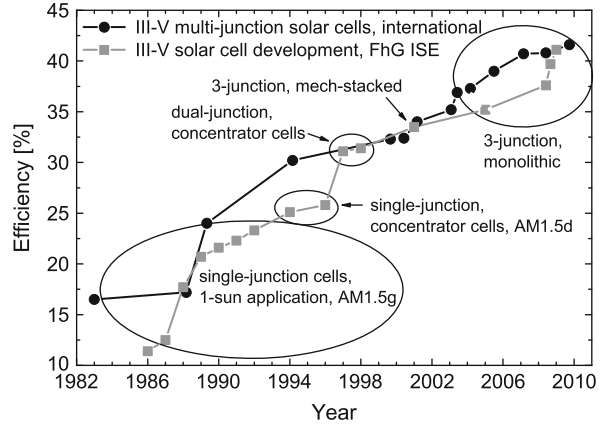
Abstract During the last years high-concentration photovoltaics (HCPV) technology has gained growing attention. Excellent operating AC-system efficiencies of up to 25% have been reported. One of the driving forces for this high system efficiency has been the continuous improvement of III–V multi-junction solar cell efficiencies. In consequence, the demand for these solar cells has risen, and strong efforts are undertaken to further increase the solar cell efficiency as well as the volume of cell output. The production capacity for multi-junction solar cells does not constitute a limitation. Already now several tens of MWp per year can be produced and the capacities can easily be increased. The state-of-the art approach for highly efficient photovoltaic energy conversion is marked by the $\text{Ga}_{0.50}\text{In}_{0.50}\text{P}/\text{Ga}_{0.99}\text{In}_{0.01}\text{As}/\text{Ge}$ structure. This photovoltaic device is today well established in space applications and recently has entered the terrestrial market. The following chapter presents an overview about the present research status in III–V multi-junction solar cells at Fraunhofer ISE regarding cell design, expected performance, numerical simulation tools, adaptation of devices to different incident spectra and the fabrication of these devices. Finally, an outlook on future developments of III–V multi-junction solar cells is given.

1.1 Introduction

There are different approaches to reduce the levelized costs of electricity from photovoltaics. On one hand, module costs decrease due to economies of scale, less material and energy consumption, or the use of cheap materials. On the other

S.P. Philipps (✉) · A.W. Bett (✉)
Fraunhofer Institute for Solar Energy Systems, Heidenhofstr. 2, 79110 Freiburg, Germany
e-mail: simon.philipps@ise.fraunhofer.de; andreas.bett@ise.fraunhofer.de

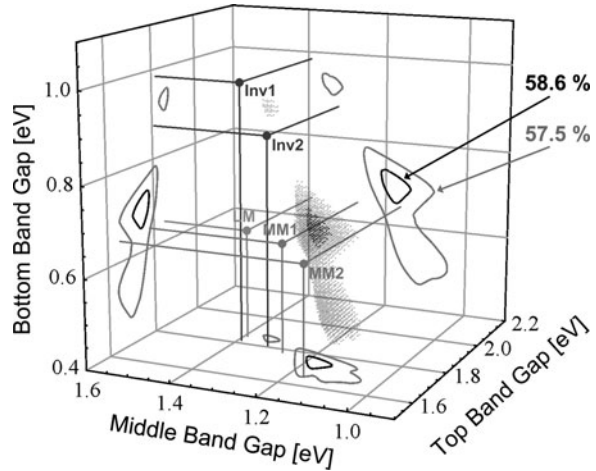
Fig. 1.1 Development of record efficiencies at Fraunhofer ISE (*squares*) and elsewhere (*circles*) for different kinds of III–V multi-junction solar cells from the 1980s to autumn 2009



hand, system costs can be reduced by an increase in module efficiency, which also provides the advantage of smaller systems and less use of area. Hence, all components of a HCPV system have to be further developed to reach highest efficiencies. Large progress can be observed, especially in the field of III–V multi-junction solar cells, where record efficiencies above 41% have been reported by different groups in 2009 [1, 2]. However, despite the high concentration levels, the solar cell still represents up to 20% of the overall costs of a HCPV system [3]. Therefore, a key element for further energy cost reduction is a highly efficient multi-junction solar cell. Multiple stacking of solar cells with growing bandgap energies increases the efficiency of the overall device since the solar spectrum is exploited more profitably. This becomes obvious when looking at the cell development of Fraunhofer ISE and other institutions from the 1980s to autumn 2009, which is summarized in Fig. 1.1. Until the middle of the 1990s, single-junction solar cells were investigated and achieved efficiencies above 25%. Then monolithic dual-junction solar cells have boosted the efficiency records above 30%. Monolithic triple-junction structures have finally surpassed the 40% mark and are still heading for higher efficiencies. In 2009 a GaAs single-junction concentrator solar cell made at Fraunhofer ISE reached a record efficiency of 29.1% under the AM1.5d ASTM G173-03 spectrum (in the following: AM1.5d) and a concentration of 117 suns (1 sun corresponds to 1 kW m^{-2}). For a monolithic III–V dual-junction solar cell, a record value of 32.6% under 1,000 suns (AM1.5d) was achieved at the UPM Madrid using $\text{Ga}_{0.51}\text{In}_{0.49}\text{P}$ and GaAs subcells [4].

However, the state-of-the-art device is a lattice-matched triple-junction solar cell consisting of monolithically stacked $\text{Ga}_{0.50}\text{In}_{0.50}\text{P}$ -, $\text{Ga}_{0.99}\text{In}_{0.01}\text{As}$ -, and Ge junctions. It has reached conversion efficiencies of 41.6% at concentrations of 364 suns under the AM1.5d spectrum [2]. Yet, detailed balance calculations [5] show that the bandgap combination of the lattice-matched design is not optimally adjusted to the solar spectrum. The GaInAs middle cell uses the smallest part of the spectrum and hence produces the lowest current $J_{\text{SC, GaInAs}}$ compared to the GaInP top cell with about 11% more current and the Ge bottom cell with about twice $J_{\text{SC, GaInAs}}$.

Fig. 1.2 Ideal efficiencies of triple-junction solar cell structures calculated with etaOpt [9] under the AM1.5d ASTM G173-03 spectrum with a concentration ratio of 500 suns and a cell temperature of 65°C



This is why different approaches for achieving current-matching conditions have been suggested [6–8]. Presently, the use of metamorphic structures as discussed below proves to be the most successful strategy.

Figure 1.2 shows how the ideal efficiency of a triple-junction solar cell design varies with the bandgap energies of the three individual junctions. This diagram has been calculated with the model etaOpt [9] (for download see [10]), which is based on the detailed balance method first introduced by Shockley and Queisser [5]. It is assumed that radiative recombination is the only recombination mechanism. Furthermore, an external quantum efficiency (EQE) of unity is assumed for each subcell. In order to improve current matching under a certain spectrum, photocurrent from upper subcells can be transferred to lower ones. In reality this is achieved by thinning the absorbing layers. In order to model this effect, each subcell has an individual degree of transparency, which can be adjusted to improve current-matching. The efficiency then is calculated according to the one-diode model. The calculations are carried out under the AM1.5d spectrum with a concentration of 500 suns and a cell temperature of 65°C. These operating conditions represent a reasonable average for today's concentrator systems. As Fig. 1.2 illustrates, the global maximum for AM1.5d lies at a bandgap combination of 1.75, 1.18, and 0.70 eV. A separated local maximum with a 2.4% (rel.) lower efficiency is found for the relatively high bandgap combination 1.86, 1.34, and 0.93 eV. This twofold maximum results from the absorption band of atmospheric water and carbon dioxide around 1,400 nm, which significantly deteriorates the efficiency of bandgap combinations in between the two maxima. Accordingly, under the extraterrestrial AM0 spectrum only a single maximum exists. Assuming that – as a rule of thumb – about 70–80% of the theoretical efficiency can be achieved in practice, the theoretical model provides a reasonable guideline to assess the potential of a solar cell design. The bandgap combinations of five specific triple-junction solar cell structures, for which efficiencies of over 40% under the concentrated AM1.5d spectrum have already been experimentally

realized, are indicated: lattice-matched $\text{Ga}_{0.50}\text{In}_{0.50}\text{P}/\text{Ga}_{0.99}\text{In}_{0.01}\text{As}/\text{Ge}$ (LM) [11–13]; metamorphic $\text{Ga}_{0.44}\text{In}_{0.56}\text{P}/\text{Ga}_{0.92}\text{In}_{0.08}\text{As}/\text{Ge}$ (MM1) [11]; metamorphic $\text{Ga}_{0.35}\text{In}_{0.65}\text{P}/\text{Ga}_{0.83}\text{In}_{0.17}\text{As}/\text{Ge}$ (MM2) [1]; inverted metamorphic $\text{Ga}_{0.50}\text{In}_{0.50}\text{P}/\text{GaAs}/\text{Ga}_{0.73}\text{In}_{0.27}\text{As}$ (Inv1); inverted (double) metamorphic device $\text{Ga}_{0.63}\text{In}_{0.37}\text{As}/\text{Ga}_{0.96}\text{In}_{0.04}\text{As}/\text{GaAs}$ (Inv2) [14].

Today, the industry standard is still the lattice-matched triple-junction solar cell, as similar structures have been developed, produced, and successfully tested for space applications [15–17]. Metamorphic or inverted concepts have not been produced in large quantities yet. Standards for the long-term stability test of such highly strained solar cell structures have to be developed and the devices have to be qualified before mass production. As the space-market is comparatively small, up to now the lattice-matched triple-junction solar cell can be purchased from only a few global suppliers, among these are AZUR SPACE Solar Power GmbH (Germany), Emcore Inc. (USA), and Spectrolab Inc. (USA).

The following section presents an overview about the actual research status on III–V-based multi-junction solar cells at Fraunhofer ISE regarding numerical device simulation as well as device fabrication. Subsequently, the possible next steps in cell design are outlined.

1.2 Research Status

In order to optimize such complex solar cell structures as multi-junction cells, numerical modeling of these devices is indispensable to reduce the number of expensive and time-consuming experiments. At Fraunhofer ISE sophisticated numerical modeling tools are used in the optimization process. The simulation is closely linked to the experimental optimization, concerning feasibility of the semiconductor structures, material quality, and evaluation of the models.

1.2.1 Numerical Simulation

The high number of layers in III–V multi-junction solar cell structures makes a pure experimental optimization very expensive and protracted. An accurate and reliable modeling is desirable to accelerate the optimization procedure considerably. However, a predictive modeling of these sophisticated structures is challenging due to the complex electrical and optical interactions between the different layers and the high number of material parameters and physical phenomena that need to be considered. In recent years, the capabilities of various approaches and tools for the simulation of III–V multi-junction solar cells have greatly improved [18–23]. In the III–V group at Fraunhofer ISE, three different approaches are used. The optimal number of bandgaps and the ideal bandgap combination is evaluated with etaOpt (see Sect. 1.1). We analyze the semiconductor layer structure with the

commercially available semiconductor simulation environment Sentaurus TCAD from Synopsys. The grid design is optimized with the circuit simulator LTSpice from Linear Technology Corporation [24]. In the following, a short overview of the status of our modeling capabilities is presented.

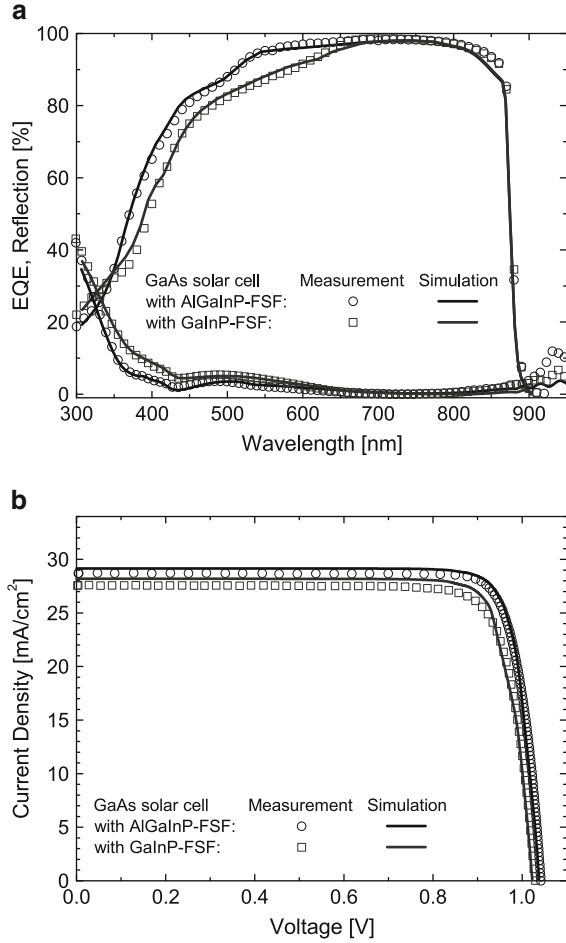
Two prerequisites have to be fulfilled to enable realistic simulations with Sentaurus TCAD: first, the necessary models describing the occurring physical phenomena need to be implemented and validated. Of particular importance for III–V multi-junction solar cells are optical interference effects, optical generation [25] and recombination of minority carriers, tunneling effects [20] and carrier transport at hetero-interfaces [26]. Second, material parameters such as optical constants, carrier mobilities, bandgap energies, electron affinity and parameters for radiative, Auger, Shockley-Read-Hall as well as interface recombination are required for each semiconductor layer in the structure. Both prerequisites are satisfactory fulfilled for the materials used in our GaAs single-junction solar cells, as well as in our lattice-matched $\text{Ga}_{0.51}\text{In}_{0.49}\text{P}$ /GaAs dual-junction solar cells. However, for other materials, especially those in metamorphic III–V multi-junction solar cells, the lack of material data limits the modeling capabilities [27]. To keep the computational effort within tolerable limits, the smallest two-dimensional symmetry element of the solar cell is modeled, which is constructed by a cut through the layers from cap to substrate perpendicular to the grid fingers. The element covers a width corresponding to half of the finger spacing to ensure that series resistance effects caused by lateral current flow in the device are taken into account.

Figure 1.3 shows a comparison between measured and simulated EQE, reflection and I–V curve of two GaAs solar cells with different material for the front surface field (FSF) layer. The model and material parameters are based on [26]. The good agreement between measurement and simulation proves the validity of the numerical model. Note that all material parameters of the solar cell except for the FSF layer have been identical. The GaInP FSF layer leads to significant absorption in the short wavelength range between 300 nm and therefore reduces the EQE. This underlines the importance of a high bandgap material for the FSF layer.

An additional challenge for the modeling of multi-junction solar is the requirement of a proper and numerically stable model for the tunnel diode, which connects the subcells in series. It was found that nonlocal interband tunnel diode models reproduce measured tunnel diode I–V curves very well in a large voltage range [20, 28]. These models cover the full nonlinearity of the tunneling mechanism and enable the simulation of multi-junction solar cells within semiconductor simulation environments. However, detailed quantum mechanical calculations propose that interband tunneling cannot explain the high currents of typical tunnel diodes for multi-junction solar cells [29]. Rather resonant tunneling through defects homogeneously distributed in the junction is identified as possible tunneling mechanism. Thus, the phenomena of tunneling in III–V multi-junction solar cells need to be investigated further in the future.

Yet, with the nonlocal interband tunnel diode model, we were able to model a lattice-matched dual-junction solar cell with a top cell of $\text{Ga}_{0.51}\text{In}_{0.49}\text{P}$ and a bottom cell of GaAs [21]. The sophisticated device contains an anti-reflection

Fig. 1.3 Comparison between measured and simulated EQE and reflection (a) and I–V curve under AM1.5g (b) for two GaAs solar cells with different front surface field (FSF) layer material. The devices with an area of 1 cm^2 were designed for operation under AM1.5g ((a) reprinted with permission from[27]. Copyright 2010 MIDE M Society)



coating of $\text{MgF}_2/\text{TiO}_2$, a $p\text{-GaAs}/n\text{-GaAs}$ Esaki interband tunnel diode, as well as a distributed Bragg reflector composed of 20 alternating layers of $\text{Al}_{0.80}\text{Ga}_{0.20}\text{As}$ and $\text{Al}_{0.10}\text{Ga}_{0.90}\text{As}$. As shown in Fig. 1.4, a good agreement is achieved between experimental and simulated EQE of top and bottom cell, reflection and I–V curve under the AM1.5g spectrum. The slight deviations in the modeled reflection for wavelengths higher than the bandgap of the bottom cell are caused by a minor inaccuracy of the transfer matrix method [25] used for the description of the optical processes. A deviation is also observable in the I–V curve in the range of 0.7 V and about 1.7 V. In contrast to the slightly increasing measured current, the simulated value remains constant. In the real device, such a current decrease can either be caused by a distributed series resistance effect along the grid fingers or by a current leakage at the cell edge. Both effects are not covered in our two-dimensional modeling approach.

The sophisticated numerical model constitutes a quick and cost-efficient tool to study the effect of structural changes on the cell performance. As illustrated in

Fig. 1.4 A good agreement is achieved between simulated and measured EQE and reflection (a) and I–V curve (b) for the investigated $\text{Ga}_{0.51}\text{In}_{0.49}\text{P}/\text{GaAs}$ dual-junction solar cell (reprinted with permission from [21]. Copyright 2008. Wiley)

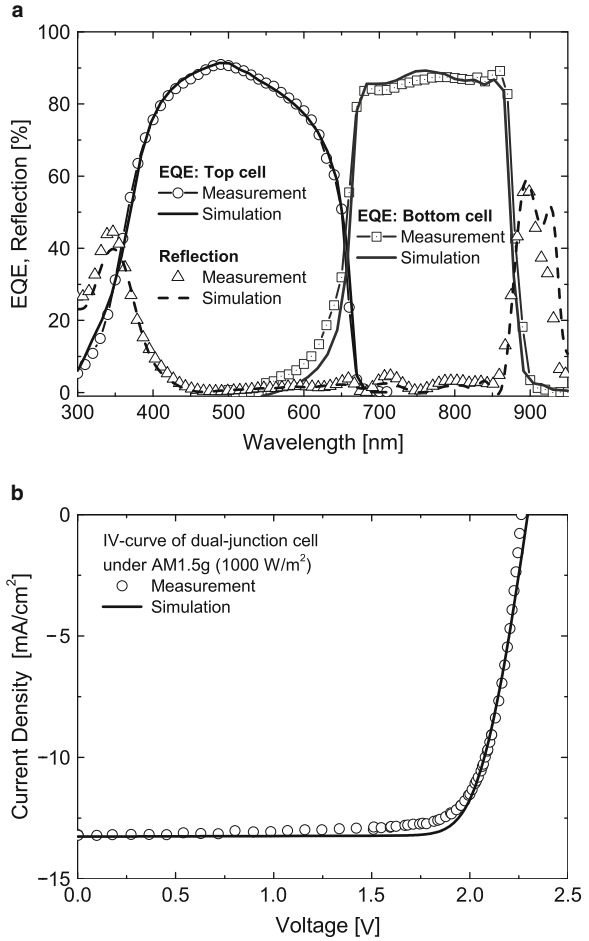


Fig. 1.5, doubling of the tunnel diode thickness strongly reduces the bottom cell's EQE. We explain this by absorption in the GaAs material of the tunnel diode. Due to the stronger absorption of high energy photons, the decrease of the EQE is more pronounced for lower wavelengths. The simulations underline that it is very important to make the tunnel diode as thin as possible if it consists of the same material as the absorber of the lower cell. In most cases, a better option is to use higher bandgap materials for the tunnel diode [30]. A further application of the recently developed numerical solar cell models is design optimization [21, 22, 27, 31].

As shown above, the semiconductor layer structure can be very well modeled with a two-dimensional symmetry element. Yet, for the optimization of the front contact grid such a model is not sufficient. In principle it would be possible to model and simulate a complete solar cell in all three dimensions within the Sentaurus TCAD simulation environment. However, due to the high number of mesh points

Fig. 1.5 Influence of the tunnel diode thickness on the EQE of a $\text{Ga}_{0.51}\text{In}_{0.49}\text{P}/\text{GaAs}$ dual-junction solar cell

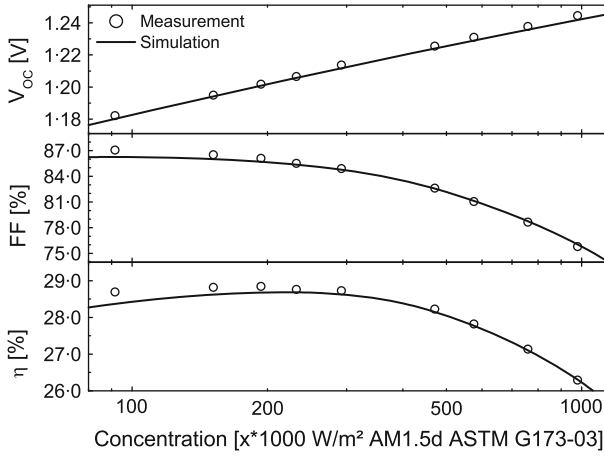
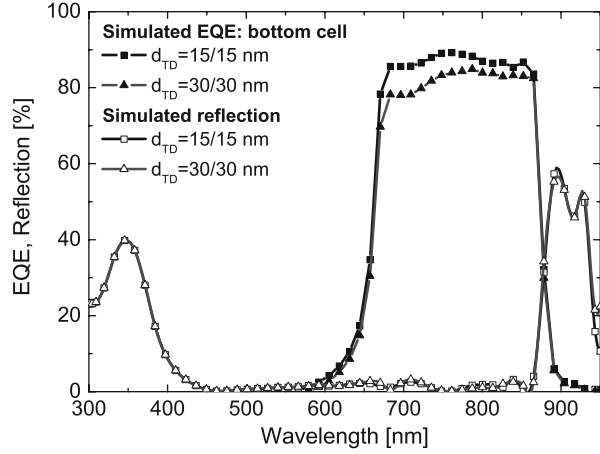


Fig. 1.6 Comparison between measured and simulated fill factor and efficiency for a GaAs concentrator solar cell with an active area of 5 mm^2 . For the simulation the SPICE network model presented by Steiner et al. [23] was used

necessary for a realistic model, the computational effort would be enormous, leading to intolerable computing time of weeks or even months. Therefore, we optimize the front contact separately with an electrical network model. The solar cell is modeled as a network of elementary cells consisting of diodes, resistances, and current sources to model the saturation currents and the photo-generated current. The elementary cells are connected in parallel through ohmic resistances representing, for instance, the lateral conducting emitter layer or the metal fingers. Thereby, a network of electrical components is created, which describes the whole solar cell. The IV-characteristic is calculated with the circuit simulator LTSpice, which uses a Simulation Program with Integrated Circuit Engineering (SPICE) approach. More details about our network model can be found in [23]. Figure 1.6 shows a comparison

between measured and simulated I–V parameters as a function of the concentration ratio for a GaAs concentrator solar cell. Measurement and simulation agree well. Note that the experimental cell reaches a high efficiency of $28.8 \pm 1.2\%$ at 230 suns under the reference spectrum AM1.5d [32]. The network modeling approach is highly predictive and has successfully been applied for the design of contact grids for different cell structures and various illumination conditions. Together with the etaOpt approach and the simulations with Sentaurus TCAD, a very powerful set of modeling tools is available. These numerical modeling techniques are now well established for supporting the design process of multi-junction solar cells.

1.2.2 Device Fabrication

In order to avoid strain and defects in the crystal structure of a multi-junction solar cell, all III–V compounds are usually grown lattice-matched to the substrate. Consequently, from the commercially available semiconductor substrates, GaAs and Ge are the most suitable for the further growth of (Al)GaInAs- and (Al)GaInP-based compounds. Considering the diagram shown in Fig. 1.2, Ge with its bandgap of 0.66 eV is the obvious choice as bottom cell in a triple-junction structure. Hence, the straightforward lattice-matched approach makes use of a $\text{Ga}_{0.50}\text{In}_{0.50}\text{P}$ top cell, a $\text{Ga}_{0.99}\text{In}_{0.01}\text{As}$ middle cell, and a Ge bottom cell. While the upper cells are commonly deposited via epitaxy, the Ge subcell is established via diffusion of group-V atoms into a *p*-doped Ge substrate. This kind of structure has been leading to 41.6% conversion efficiency [23]. However, this lattice-matched structure appears to be quite far away from the optimum bandgap configuration (see Fig. 1.2) and is highly current-mismatched. Lower bandgap materials are required for the upper subcells. This can be achieved by increasing the indium content in the top and middle cell. With the almost ideal bandgaps of 1.67 eV for GaInP and 1.18 eV for GaInAs, the metamorphic triple-junction solar cell approach approximates the optimum configuration. However, the higher In-content in the upper subcells also increases the lattice-constant of these materials. The combination of $\text{Ga}_{0.35}\text{In}_{0.65}\text{P}$, $\text{Ga}_{0.83}\text{In}_{0.17}\text{As}$, and Ge causes a high lattice-mismatch of 1.1% between the Ge and the upper two subcells, while the top and middle subcell are lattice-matched to each other. This metamorphic cell structure (Fig. 1.2, MM2) was developed at Fraunhofer ISE [1, 8, 12, 33].

Figure 1.7 illustrates the difference between the lattice-matched and the metamorphic concept. The larger lattice constant of the upper subcells requires a transition region from the lattice constant of Ge to the lattice constant of $\text{Ga}_{0.83}\text{In}_{0.17}\text{As}$. This transition is realized by a metamorphic buffer structure.

We have developed an optimized step-graded buffer structure made from $\text{Ga}_{1-y}\text{In}_y\text{As}$ to overcome the high mismatch in the lattices. This buffer increases the lattice constant as required, reduces the amount of residual strain to a minimum of only 6–9%, and avoids the penetration of threading dislocations into the middle and top cell. The degree of strain relaxation of an epitaxial semiconductor layer with cubic lattice is defined as the ratio of the in-plane lattice constant to the lattice

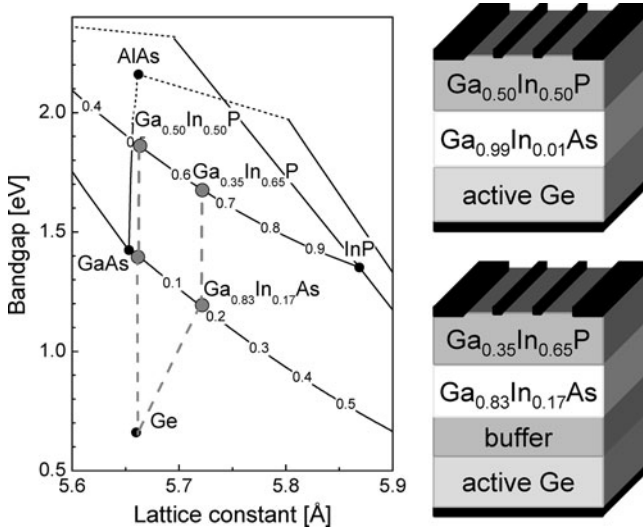
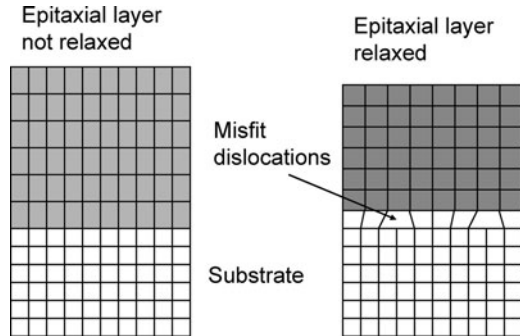


Fig. 1.7 Relation between bandgap and lattice constant for different binary (black dots) and ternary (lines) semiconductor materials as well as for germanium (left). The triple-junction solar cell lattice-matched to Ge features a $\text{Ga}_{0.99}\text{In}_{0.01}\text{As}$ middle cell and a $\text{sGa}_{0.50}\text{In}_{0.50}\text{P}$ top cell (top right structure). The $\text{Ga}_{0.83}\text{In}_{0.17}\text{As}$ and the $\text{Ga}_{0.35}\text{In}_{0.65}\text{P}$ subcell of a metamorphic triple-junction solar cell (bottom right structure) are lattice-matched to each other, but have a 1.1% mismatch to the substrate. This mismatch is managed by a buffer structure

Fig. 1.8 Schematic illustration of a pseudo-morphically strained layer (left) grown on a substrate with smaller lattice constant. As a critical thickness is exceeded, the strained epitaxial layer starts to relax by the generation of misfit dislocation (right)



constant of the relaxed lattice normalized by the lattice constant of the substrate. Figure 1.8 schematically illustrates the process of strain relaxation of a strained epitaxial layer. Up to a critical thickness, first defined by Matthews et al. [34], the layer is pseudo-morphically strained. As the layer thickness increases beyond the critical thickness, first misfit dislocations are generated within the interface due to bending of pre-existing substrate dislocations. With a further increase of the layer thickness, several generation mechanisms for misfit dislocation set in, which finally lead to a significant strain relaxation [35, 36].

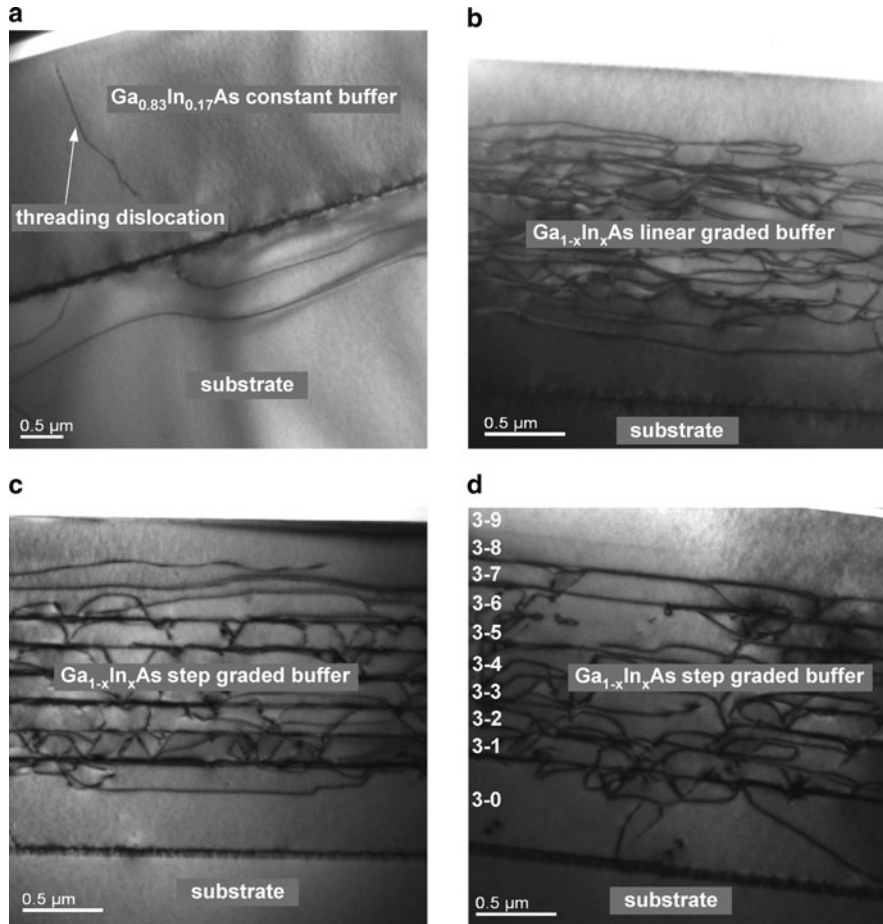


Fig. 1.9 TEM cross-section images from a constant buffer with abrupt change in lattice constant (a), a linearly graded buffer with linear change in lattice constant (b), a step graded buffer with about seven grading steps (c), and a step graded metamorphic Ga_{1-x}In_xAs buffer with increasing In content from 1% to 17% (3-1 to 3-7) and an overshooting layer (3-8) with 23% In (d). (TEM images measured at the Christian-Albrechts-University in Kiel, Germany)

Figure 1.9 shows TEM cross-section images of different buffer concepts which we have investigated: a constant buffer (a), a linearly graded buffer (b), and two step graded buffers (c and d). In contrast to the graded structures, the constant buffer growth leads to the generation of a large number of threading dislocations which may act as recombination centers in the photoactive region of the multi-junction solar cells. For high performance devices threading dislocation densities below 10^6 cm^{-2} are necessary. According to our experience, this can only be achieved with the graded buffers. Especially the step graded buffer localizes the dislocations generated within the interface regions between the steps and prevents the generation

of threading dislocations, penetrating into the photoactive regions of the solar cell structure. This is the reason for the success of these buffer structures.

A more detailed development of the step graded buffers enables the reduction of remaining strain to a minimum of only 6–9%. This is achieved by triggering the strain-relaxation of the upper part of the buffer by introducing an overshooting $\text{Ga}_{1-x}\text{In}_x\text{As}$ layer with even larger lattice constant than originally intended ($x > 0.17$). The subsequent growth continues with the lattice constant of $\text{Ga}_{0.83}\text{In}_{0.17}\text{As}$. The degree of strain relaxation can be adjusted by the thickness of the overshooting layer and by the strength of overshooting. Figure 1.9d shows a TEM cross-section image of a buffer consisting of seven $\text{Ga}_{1-x}\text{In}_x\text{As}$ grading steps from 1% In to 17% In followed by an overshooting layer with 23% In. With this structure, the remaining strain in the following layers is reduced to about 6–9%.

The remaining strain of a metamorphic triple-junction solar cell structure can be reduced considerably. However, in situ collected data show that the $300\text{ }\mu\text{m}$ thick Ge-wafers bend during growth. Figure 1.10 shows the curvature transients from in situ measurement during the growth process for different buffer structures with relaxations between 81% and 94%. The first highly strained layers of the buffer cause a strong increase in curvature. As relaxation sets in, the curvature remains almost constant. The remaining value is proportional to the remaining strain in the structure. Experiments also show that thinner wafers in the range of $150\text{ }\mu\text{m}$ are unsuitable for metamorphic structures, since the even stronger bending of the substrate affects growth on the wafer. Today, different extensions to the step graded buffer concepts are under investigation. Additional blocking layers made from hard materials such as GaInNAs can be deposited over the buffer structure to bend the threading dislocations from growth direction into the growth plane [37]. This allows even less dislocations to penetrate into the photoactive regions of the structure. Adding aluminium to the $\text{Ga}_{1-x}\text{In}_x\text{As}$ alloy increases its bandgap and hence renders the buffer more transparent. This may be important to increase the current generated by the Ge subcell.

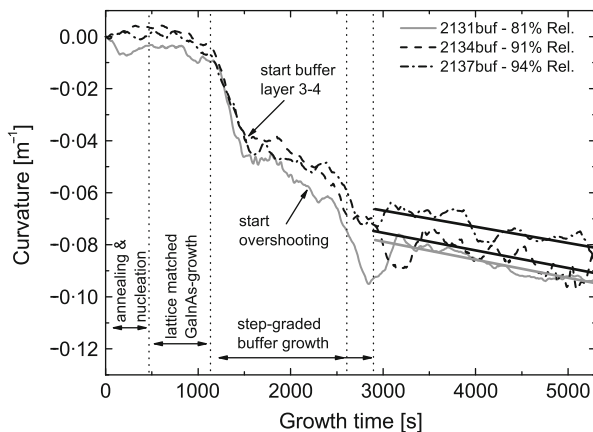


Fig. 1.10 In situ measured curvature of the wafer during growth of different metamorphic triple-junction solar cell structures. The different buffers result in remaining strain between 19% and 6%. This correlates with the remaining values in curvature

In lattice-matched as well as in metamorphic multi-junction solar cells, the individual subcells are interconnected via interband tunnel diodes, which provide a low electric resistance and can be designed transparent for light converted in the following subcell. Tunnel diodes essentially consist of two degenerately doped layers with different polarity. High n -doping levels in the range of 10^{19} cm^{-3} have been achieved with tellurium or silicon in GaInAs or GaInP. Very high p -doping in the range of 10^{20} cm^{-3} is achieved with carbon in AlGaAs [38]. Tunnel current densities above 100 A cm^{-2} have been measured. However, tunnel diodes in metamorphic solar cells need larger lattice constants, which can be realized by adding In to the mentioned compounds, as already done for the subcells. But the carbon doping of such AlGaInAs layers turns out to be more difficult. The commonly used carbon precursor CBr_4 cannot be used anymore as it etches indium [38]. Intrinsic C -doping from the alkyl groups of TMAI had been applied, but the doping levels achieved are one order of magnitude lower than with In-free AlGaAs. The use of lattice-mismatched layers in the tunnel diode, such as AlGaAs, generates dislocations, which degrade the solar cell structure. This is why we designed strain compensated tunnel diodes. These structures make use of a highly doped AlGaAs layer, which has a too small lattice constant and causes tensile strain in the tunnel diode structure. In order to reduce this strain, a neighboring layer such as GaInAs or GaInP is grown with a too large lattice constant. This compensates the strain in the structure and avoids the generation of dislocations. Figure 1.11 illustrates this concept with a p -AlGaAs/ n -GaInAs tunnel diode. Due to strain compensation, the rest of the structure is not affected by the highly strained tunnel diodes.

As explained above, the subcells of a metamorphic triple-junction solar cell are almost ideally adapted to the AM1.5d spectrum. Figure 1.12 compares the EQEs of such a structure with a lattice-matched triple-junction cell. The lower bandgaps in the metamorphic cell shift the EQEs to higher wavelengths. The favorable bandgap combination together with the improvements regarding the metamorphic buffer and the tunnel diodes are the key points that lead to an efficiency of 41.1% with our metamorphic triple-junction solar cell (Fig. 1.12).

The performance of a concentrator solar cell also strongly depends on the cell design including size, grid structure, and intended operation illumination intensity. Figure 1.13 illustrates how different front side grid layouts with decreasing amount of metallization shift the maximum efficiency to lower concentrations as shading is reduced. Furthermore, the absolute efficiency maximum rises with decreased

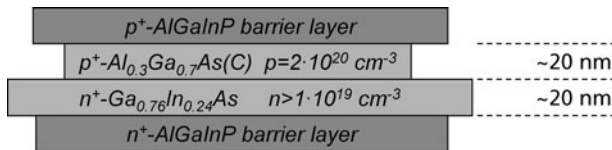


Fig. 1.11 Schematic illustration of a strain compensated tunnel diode. The width of the boxes represents the lattice constant. A compressively strained GaInAs layer is compensated with a tensile AlGaAs layer

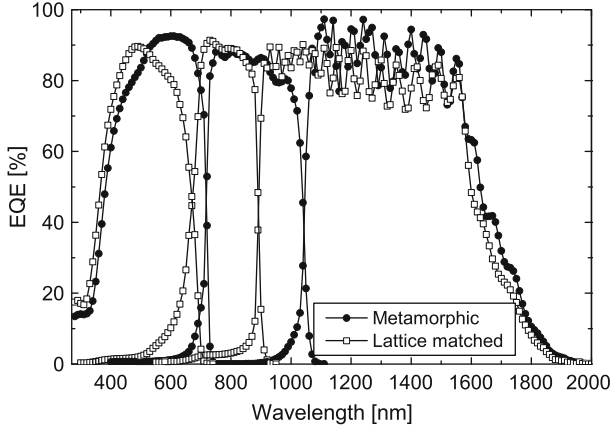


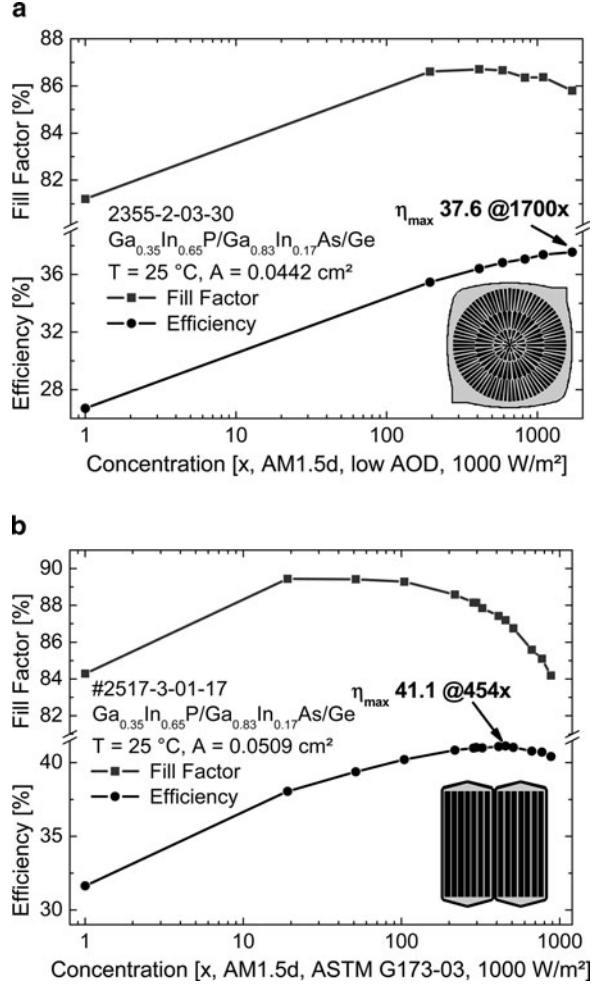
Fig. 1.12 External quantum efficiencies of a lattice-matched $\text{Ga}_{0.50}\text{In}_{0.50}\text{P}/\text{Ga}_{0.99}\text{In}_{0.01}\text{As}/\text{Ge}$ as well as a metamorphic $\text{Ga}_{0.35}\text{In}_{0.65}\text{P}/\text{Ga}_{0.83}\text{In}_{0.17}\text{As}/\text{Ge}$ triple-junction solar cell

shading. Note that the logarithmic increase of efficiency with illumination intensity is caused by an increase in open circuit voltage and in fill factor. For higher concentration ratios, more metallization is required to carry the high current densities generated. At Fraunhofer ISE, we have developed a network simulation tool to compare and optimize the size and front contact layout for various solar cell structures and different illumination intensities (see Sect. 1.2.1) [23]. Generally a small cell requires less metallization for the same resistive losses as a larger cell and thus achieves higher theoretical efficiencies because of less shading losses. In summary, this section shows that lattice-matched and metamorphic triple-junction solar cell concepts have surpassed the 41% mark and offer even further potential to increase the conversion efficiency toward 45%.

1.3 Next Steps

In recent years, research efforts for the development of III–V multi-junction solar cells with more than three subcells have significantly grown as an increase in cell efficiency is expected [2, 39–41]. It is a well-known fact that the ideal efficiency of a multi-junction solar cell under a certain spectrum increases with the number of pn -junctions [40, 42]. However, multi-junction solar cells are also known to be highly sensitive to changes in the solar spectrum [43, 44]. In terrestrial applications, the spectral distribution of the incident light strongly varies throughout day and year. In addition, the irradiance conditions can change significantly with the intended place of operation. As the sensitivity to spectral variations increases with the number of subcells, it is important to investigate the possible gain in energy production before a decision is made on which number of subcells and which material combination to realize.

Fig. 1.13 Fill factor and efficiency of two metamorphic triple-junction solar cells as a function of the concentration. Different front side metallization, which is shown in the photographs, leads to different maximum positions. The cell in (a) is suitable for high concentration ratios well above 1,000 suns, the cell in (b) is adapted for 500 suns



For this purpose, we have developed a theoretical energy harvesting model [45], in which the solar cell is modeled according to the detailed balance model etaOpt (see Sect. 1.1). Here, we investigate the energy harvesting at two locations on Earth with distinct spectral conditions: Solar Village in Saudi Arabia with rather red-rich incident light and La Parguera in Puerto Rico with a higher share of blue light. For these places, measured atmosphere parameters from the AERONET database [46] are used to calculate direct solar spectra with the computer code SMARTS 2.9.5 [47–49]. A discretization of one spectrum per hour was chosen resulting in more than 4,400 spectra for each geographical location. Concerning the operating conditions, we assume a concentration factor of 1,000 suns, which is expected to become standard for future concentrator systems. In addition, a constant cell temperature of 338 K is assumed. From our experiences, this value represents a reasonable average, which is also used by other groups [50]. Based on the simulated

spectra the annual sum of the produced energy, which is computed from the produced energy for each day in the year, is calculated and is then referred to the irradiated energy. The overall annual incident energies are $2,599 \text{ kWh m}^{-2} \text{ a}^{-1}$ at Solar Village and $2,849 \text{ kWh m}^{-2} \text{ a}^{-1}$ at La Parguera. The ratio of the energy produced to the irradiated energy defines the energy harvesting efficiency.

III–V multi-junction concentrator solar cells are usually optimized and rated under the reference spectrum AM1.5d. Following this approach, we first calculated the ideal bandgap combination under the reference spectrum (1,000 suns, 338 K) for solar cells with 1–6 subcells. Then the energy harvesting efficiencies of the resulting bandgap designs at Solar Village (Fig. 1.14a) and La Parguera (Fig. 1.14b) were calculated. The results correspond to the left bars in each figure. The right bars indicate the energy harvesting efficiencies that could be realized with the optimal bandgap combination for the intended place of operation. These were determined

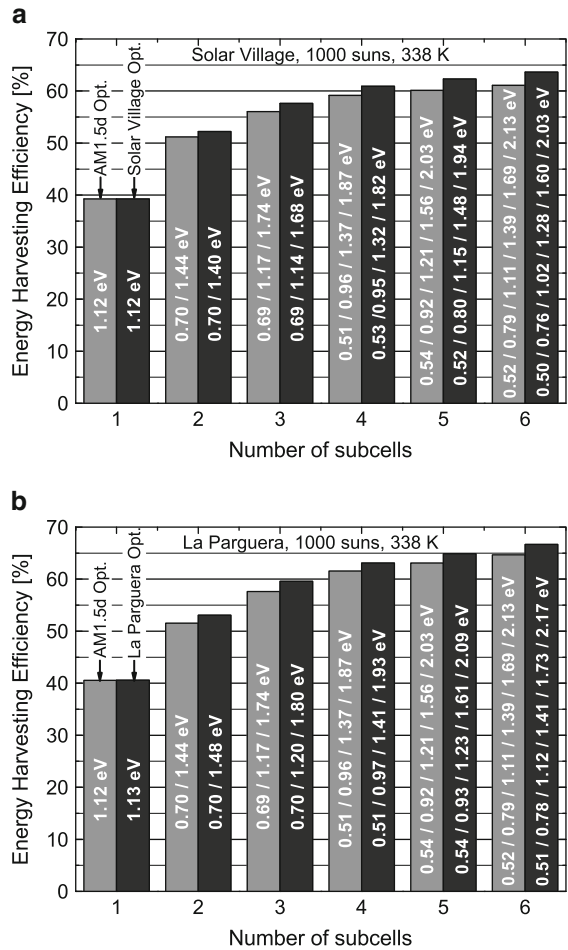


Fig. 1.14 Comparison of the maximum energy harvesting efficiency versus the number of subcells at Solar Village, Saudi Arabia (a) and La Parguera, Puerto Rico (b). The indicated bandgap combinations result from the optimization of the cell efficiency under the reference spectrum AM1.5d ASTM G173-03 (left bars), and of the energy harvesting efficiency for the intended place of operation (right bars)

by maximizing the yearly produced energy based on the more than 4,400 spectra for Solar Village or La Parguera, respectively.

It is noteworthy that the energy harvesting efficiency increases with the number of subcells in all cases despite the considered spectral variations throughout day and year. However, the relative gain of adding additional junctions is small for more than four junctions. Compared to the bandgap combinations resulting from the optimization of the cell efficiency under the reference spectrum AM1.5d, a rather strong increase in energy harvesting efficiency can be realized with the optimal bandgap combinations for each location. However, these bandgap combinations go into different directions. At Solar Village, slightly lower bandgaps are favorable due to the low share of blue light at this location. In contrast, higher bandgaps are favorable under the blue-rich spectral conditions of La Parguera. It should be noted that the detailed balance model assumes ideal solar cells. As a rule of thumb 70–80% of the theoretical cell efficiencies can be achieved in practice. However, the realization of good material quality usually becomes more challenging for solar cells with a higher number of subcells due to the greater complexity of the structure and the novel materials involved (see discussion below). Thus, it is still an open question if solar cells with more than four *pn*-junctions can be realized with sufficient material quality to harvest the small relative gains predicted by our energy harvesting model.

Figure 1.15 summarizes the development roadmap for III–V multi junction solar cell concepts investigated at Fraunhofer ISE. Apart from the already discussed lattice-matched (a) and metamorphic (d) triple-junction solar cells, different

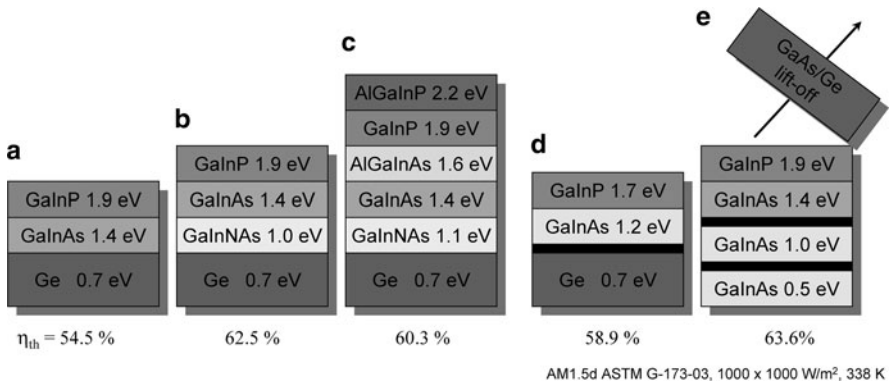
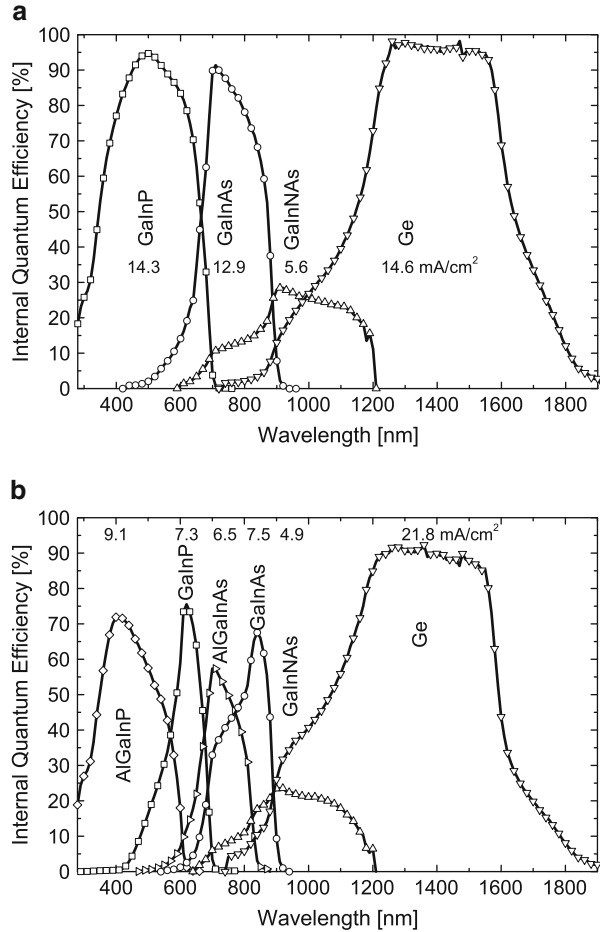


Fig. 1.15 Roadmap for the development of III–V multi-junction solar cells at Fraunhofer ISE and corresponding maximum efficiencies calculated with etaOpt (AM1.5d, 1,000 suns, 338 K). The number of junctions and the efficiency of the lattice-matched GaInP/GaInAs/Ge approach (a) can be increased by adding a GaInNAs subcell (b). As the performance of this device is limited by the diffusion length in GaInNAs, a six-junction cell has been designed (c). An almost ideal bandgap combination is achieved with a metamorphic triple-junction solar cell (d). Adding a second buffer leads to a metamorphic quadruple-junction solar cell (e). In order to grow as many junctions as possible lattice-matched to the substrate, the structure is grown inverted

Fig. 1.16 Measured internal quantum efficiency of a four-junction (a) and a six-junction solar cell (b), which were produced at Fraunhofer ISE. The subcells' short circuit current densities are also indicated



concepts with more than three subcells are under investigation. The concepts can be divided into two groups. The first group uses materials that can be grown lattice-matched on germanium substrates (a–c). The second group includes buffer structures to enable the use of metamorphic materials (d–e). For a lattice-matched approach on a Ge substrate, a strong increase in efficiency is expected from the inclusion of a fourth junction with a bandgap of about 1 eV (b), which may be realized with the quaternary alloy GaInNAs [51]. The (a) diagram in Fig. 1.16 shows the internal quantum efficiency (IQE) of such a device produced at Fraunhofer ISE. The GaInNAs subcell limits the current due to the quite low minority diffusion lengths, which are very likely caused by the formation of nitride chains. A lot of work is done to solve this deficiency. One promising method is to use thermal annealing to dissolve the nitride chains [52].

Another way to get around the low diffusion length is to increase the number of subcells. In a six-junction device, each subcell produces a smaller current than in a

quadruple cell and hence the subcells are thinner. Thus, shorter diffusion lengths are acceptable. A six-junction cell may be realized by adding AlGaInP and AlGaInAs subcells to the stack (Fig. 1.15c). The graph (b) in Fig. 1.16 shows the IQE of such a six-junction solar cell. The Ge bottom cell has a quite high current due to the not ideal bandgap combination of this device. Smaller bandgaps for the lower cells would be favorable. A way to realize such combinations is to use more than one lattice-transition buffer and to grow the stack inversely (Fig. 1.15e).

This chapter showed that III–V triple-junction solar cells have reached efficiencies of 41.6% under concentrated sunlight [2]. We expect that the record efficiency of these devices will soon reach above 43%. For even higher efficiencies toward 50% III–V multi-junction solar cells with more than three subcells are promising.

References

1. W. Guter, J. Schöne, S.P. Philipps, M. Steiner, G. Siefert, A. Wekkeli, E. Welser, E. Oliva, A.W. Bett, F. Dimroth, *Appl. Phys. Lett.* **94**(22), 223504 (2009)
2. R.R. King, A. Boca, W. Hong, D. Larrabee, K.M. Edmondson, D.C. Law, C.M. Fetzer, S. Mesropian, N.H. Karam, in *Conference Record of the 24th European Photovoltaic Solar Energy Conference and Exhibition*, Hamburg, Germany, 21–25 Sep 2009, pp. 55–61
3. H. Lerchenmüller, A.W. Bett, J. Jaus, G. Willeke, in *Conference Record of the 3rd International Conference on Solar Concentrators for the Generation of Electricity or Hydrogen*, Scottsdale, AZ, USA, 1–5 May 2005, p. 6.
4. I. García, I. Rey-Stolle, B. Galiana, C. Algora, *Appl. Phys. Lett.* **94**(5), 053509 (2009)
5. W. Shockley, H.J. Queisser, *J. Appl. Phys.* **32**(3), 510 (1961)
6. D.J. Friedman, J.F. Geisz, S.R. Kurtz, J.M. Olson, *J. Cryst. Growth* **195**(1–4), 409 (1998)
7. K.W.J. Barnham, I. Ballard, J.P. Connolly, N.J. Ekins-Daukes, B.G. Klufftinger, J. Nelson, C. Rohr, *Phys. E-Low-Dimensional Syst. Nanostructures* **14**(1–2), 27 (2002)
8. A.W. Bett, C. Baur, F. Dimroth, J. Schöne, *Mater. Photovoltaics* **836**, 223 (2005)
9. G. Létay, A.W. Bett, in *Conference Record of the 17th European Photovoltaic Solar Energy Conference and Exhibition. WIP-Renewable Energies*, Munich, Germany, 22–26 Oct 2001, pp. 178–180
10. G. Létay, A.W. Bett, etaOpt, www.ise.fraunhofer.de/downloads/software/etaOpt.zip/view (2001)
11. R.R. King, D.C. Law, K.M. Edmondson, C.M. Fetzer, G.S. Kinsey, H. Yoon, R.A. Sherif, N.H. Karam, *Appl. Phys. Lett.* **90**(18), 183516 (2007)
12. F. Dimroth, *Phys. Status Solidi C – Curr. Top. Solid State Phys.* **3**(3), 373 (2006)
13. M. Yamaguchi, T. Takamoto, K. Araki, *Sol. Energ. Mater. Sol. Cell.* **90**(18–19), 3068 (2006)
14. J.F. Geisz, D.J. Friedman, J.S. Ward, A. Duda, W.J. Olavarria, T.E. Moriarty, J.T. Kiehl, M.J. Romero, A.G. Norman, K.M. Jones, *Appl. Phys. Lett.* **93**(12), 123505 (2008)
15. R.R. King, C.M. Fetzer, D.C. Law, K.M. Edmondson, H. Yoon, G.S. Kinsey, D.D. Krut, J.H. Ermer, P. Hebert, B.T. Cavicchi, N.H. Karam, in *Conference Record of the 2006 IEEE 4th World Conference on Photovoltaic Energy Conversion*, Waikoloa, HI, 17–12 May 2006, pp. 1757–1762
16. P.R. Sharps, A. Comfeld, M. Stan, A. Korostyshevsky, V. Ley, B. Cho, T. Varghese, J. Diaz, D. Aiken, in *Conference Record of the PVSC: 2008 33rd IEEE Photovoltaic Specialist Conference*, San Diego, USA, 11–16 May 2008, pp. 2046–2051
17. A.W. Bett, F. Dimroth, W. Guter, R. Hoheisel, E. Oliva, S.P. Philipps, J. Schöne, G. Siefert, M. Steiner, A. Wekkeli, E. Welser, M. Meusel, W. Köstler, G. Strobl, in *Conference Record of the 24th European Photovoltaic Solar Energy Conference and Exhibition*, Hamburg, Germany, 21–25 Sep 2009, pp. 1–6

18. S. Michael, Sol. Energ. Mater. Sol. Cell. **87**(1–4), 771 (2005)
19. Z. Li, G. Xiao, Z. Li, High Low Concentration Sol. Electric Appl. **6339**, 633909 (2006)
20. M. Hermle, G. Létay, S.P. Philipps, A.W. Bett, Progr. Photovoltaics **16**(5), 409 (2008)
21. S.P. Philipps, M. Hermle, G. Létay, F. Dimroth, B.M. George, A.W. Bett, Phys. Status Solidi-Rapid Res. Lett. **2**(4), 166 (2008)
22. M. Baudrit, C. Algora, Phys. Status Solidi a-Appl. Mater. Sci. **207**(2), 474 (2010)
23. M. Steiner, S.P. Philipps, M. Hermle, A.W. Bett, F. Dimroth, Progr. Photovoltaics **19**(1), 73 (2011)
24. LTSpice, Switcher CAD III/LT Spice. Tech. rep., Linear Technology Cooperation (2007)
25. G. Létay, M. Bresselge, A.W. Bett, in *Conference Record of the 3rd World Conference on Photovoltaic Energy Conversion*, Osaka, Japan, 11–18 May 2003, pp. 741–744
26. G. Létay, M. Hermle, A.W. Bett, Progr. Photovoltaics **14**(8), 683 (2006)
27. S.P. Philipps, W. Guter, M. Steiner, E. Oliva, G. Siefer, E. Welser, B. George, M. Hermle, F. Dimroth, A.W. Bett, Informacije MIDEA- J. Microelectron. Electron. Compon. Mater. **39**(4), 201 (2010)
28. M. Baudrit, C. Algora, in *Conference Record of the PVSC: 2008 33rd IEEE Photovoltaic Specialist Conference*, San Diego, USA, 11–16 May 2008, pp. 576–580
29. K. Jandieri, S.D. Baranovskii, O. Rubel, W. Stolz, F. Gebhard, W. Guter, M. Hermle, A.W. Bett, J. Appl. Phys. **104**(9), 094506 (2008)
30. T. Takamoto, M. Kaneiwa, M. Imaizumi, M. Yamaguchi, Progr. Photovoltaics **13**(6), 495 (2005)
31. S.P. Philipps, M. Hermle, G. Létay, W. Guter, B.M. George, F. Dimroth, A.W. Bett, in *Conference Record of the 23rd European Photovoltaic Solar Energy Conference and Exhibition*, Valencia, Spain, 1–5 Sep 2008, pp. 90–94
32. M.A. Green, K. Emery, Y. Hishikawa, W. Warta, Progr. Photovoltaics **17**(5), 320 (2009)
33. F. Dimroth, R. Beckert, M. Meusel, U. Schubert, A.W. Bett, Progr. Photovoltaics **9**(3), 165 (2001)
34. J.W. Matthews, A.E. Blakeslee, J. Cryst. Growth **27**, 118 (1974)
35. D.D. Perovic, D.C. Houghton, in *Microscopy of Semiconducting Materials* ed. by A.G. Cullis, A.E. Staton-Bevan. Conference on Microscopy of Semiconducting Materials, 20–23 Mar 1995, pp. 117–134 (Oxford, England, 1995)
36. F.K. Legoues, B.S. Meyerson, J.F. Morar, P. Kirchner, J. Appl. Phys. **71**(9), 4230 (1992)
37. J. Schöne, E. Spiecker, F. Dimroth, A.W. Bett, W. Jäger, Appl. Phys. Lett. **92**(8), 081905 (2008)
38. W. Guter, F. Dimroth, J. Schöne, S.P. Philipps, A.W. Bett, in *Conference Record of the 22th European Photovoltaic Solar Energy Conference and Exhibition*, Milan, Italy, 3–7 Sep 2007, pp. 122–125
39. D.J. Friedman, J.F. Geisz, A.G. Norman, M.W. Wanlass, S.R. Kurtz, in *Conference Record of the 2006 IEEE 4th World Conference on Photovoltaic Energy Conversion*, Waikoloa, HI, 07–02 May 2006, pp. 598–602
40. F. Dimroth, S. Kurtz, MRS Bull. **32**(3), 230 (2007)
41. M. Yamaguchi, K.I. Nishimura, T. Sasaki, H. Suzuki, K. Arafune, N. Kojima, Y. Ohsita, Y. Okada, A. Yamamoto, T. Takamoto, K. Araki, Sol. Energ. **82**(2), 173 (2008)
42. S. Kurtz, D. Myers, W.E. McMahon, J. Geisz, M. Steiner, Progr. Photovoltaics **16**(6), 537 (2008)
43. M. Meusel, R. Adelhelm, F. Dimroth, A.W. Bett, W. Warta, Progr. Photovoltaics **10**(4), 243 (2002)
44. S. Kurtz, J.M. Olson, P. Faine, Sol. Cell. **30**(1–4), 501 (1991)
45. S.P. Philipps, G. Perharz, R. Hoheisel, T. Hornung, N.M. Al-Abbadi, F. Dimroth, A.W. Bett, Sol. Energ. Mater. Sol. Cell. **94**(5), 869 (2010)
46. International AERONET Federation, AERONET (AErosol RObotic NETwork) program, aeronet.gsfc.nasa.gov (2009)
47. C. Gueymard, Sol. Energ. **71**(5), 325 (2001)
48. C. Gueymard. Simple Model of the Atmospheric Radiative Transfer of Sunshine (SMARTS), Version 2.9.5, www.nrel.gov/rredc/smarts (2009)

49. C. Gueymard, SMARTS: Simple Model of the Atmospheric Radiative Transfer of Sunshine: Algorithms and Performance Assessment. Tech. Rep. FSEC-PF-270-95, Florida Solar Energy Center, 1679 Clearlake Rd., Cocoa, FL, USA (1995)
50. G.S. Kinsey, K.M. Edmondson, Prog. Photovoltaics **17**(5), 279 (2009)
51. M. Kondow, K. Uomi, A. Niwa, T. Kitatani, S. Watahiki, Y. Yazawa, Jpn. J. Appl. Phys. Part I Regular Papers Short Notes Rev. Papers **35**(2B), 1273 (1996)
52. K. Volz, T. Torunski, O. Rubel, W. Stolz, J. Appl. Phys. **104**(5), 053504 (2008)

Next Generation of Photovoltaics

New Concepts

Cristobal, A.; Martí Vega, A.; Luque López, A. (Eds.)

2012, XVI, 356 p., Hardcover

ISBN: 978-3-642-23368-5